Chemical Science

EDGE ARTICLE

View Article Online
View Journal | View Issue



Cite this: *Chem. Sci.*, 2024, **15**, 17397

All publication charges for this article have been paid for by the Royal Society of Chemistry

Received 3rd June 2024
Accepted 18th September 2024

DOI: 10.1039/d4sc03643c

rsc.li/chemical-science



# Visualization of drug release in a chemo-immunotherapy nanoplatform *via* ratiometric $^{19}$F magnetic resonance imaging†

Fanqi Liu, Xindi Li, Yumin Li, Suying Xu, Chang Guo* and Leyu Wang*

Visualization of drug release *in vivo* is crucial for improving therapeutic efficacy and preventing inappropriate medication dosing, yet, challenging. Herein, we report a pH-activated chemo-immunotherapy nanoplatform with visualization of drug release *in vivo* by ratiometric $^{19}$F magnetic resonance imaging ($^{19}$F MRI). This nanoplatform consists of ultra-small histamine-modified perfluoro-15-crown-5-ether (PFCE) nanodroplets loaded with doxorubicin (Dox), which are packaged in trifluoromethyl-containing metal–organic assemblies *via* coordination-driven self-assembly. The chemical shifts of two types of $^{19}$F atoms in the nanoplatform are significantly different in $^{19}$F nuclear magnetic resonance (NMR) spectra, which facilitates the implementation of ratiometric $^{19}$F MRI without any signal crosstalk. In an acidic tumor microenvironment, this nanoplatform gradually degrades, which results in a sustained drug release with a real-time change in the ratiometric $^{19}$F MRI signal. Therefore, a linear correlation between the Dox release profile and ratiometric $^{19}$F MRI signal is established to visualize Dox release. Moreover, the pH-triggered disassembly of the nanoplatform leads to cell pyroptosis, which evokes immunogenic cell death (ICD), resulting in the regression of the primary tumor and inhibition of distal tumor growth. This study provides the proof-of-concept application of ratiometric $^{19}$F MRI to visualize drug release *in vivo*.

## Introduction

In the past few decades, stimulus-responsive (pH,[1,2] enzymes,[3,4] redox changes,[5,6] *etc.*) drug delivery systems have been rapidly developed due to the flourishing advancements of nanotechnology,[7–9] however, *in vivo* exact monitoring of drug release is still challenging in spite of significant progress.[10–15] Ratiometric fluorescence[16–18] and ratiometric photoacoustic[19] imaging, which can eliminate the shortcomings often encountered in single wavelength imaging by self-calibration using two responsive signals at two separate wavelengths, offers the opportunity to reproducibly measure drug release, despite some disadvantages such as limited tissue penetration depth[20] and undesirable tissue autofluorescence.[21]

Fluorine magnetic resonance imaging ($^{19}$F-MRI)[22–24] not only provides the advantages of $^{1}$H-MRI such as high spatial resolution and deep tissue penetration,[25–29] but also demonstrates virtually zero background interference,[30,31] allowing *in vivo* quantitative analysis.[32–34] Due to the diffusion and distribution of the nanoprobes *in vivo*, the $^{19}$F MRI signal intensity may be influenced by the concentration of nanoprobes. Consequently, relying solely on the absolute signal intensity of nanoprobes for imaging may inaccurately visualize drug release. Ratiometric measurement involves the self-calibration of the signal intensity by recording fluctuations in two signals, where one signal serves as a reference for normalizing another.[35,36] This method is unaffected by local nanoprobe concentration, thereby enabling more precise and reliable quantification. Employing a ratiometric method, where two distinct MR acquisitions collect images from a single sample, holds the potential for improving the efficiency of MRI.[37] Inspired by ratiometric fluorescent and ratiometric photoacoustic imaging sensors that rely on two emission bands, we attempt to develop ratiometric $^{19}$F MRI nanoprobes with two distinct $^{19}$F NMR peaks. The wide chemical shift range (>350 ppm) in $^{19}$F NMR spectroscopy enables $^{19}$F MRI probes with distinct $^{19}$F chemical shift peaks, leading to multicolor $^{19}$F MRI images and laying the foundation for ratiometric imaging. To obtain highly sensitive $^{19}$F-MRI probes for practical *in vivo* MRI applications, it is highly important but faces great challenges to increase the number of fluorine atoms in the MRI probes, meanwhile maintaining good molecular mobility and thus a high $^{19}$F MRI signal. Despite great efforts, very little has been achieved *in vivo* quantitative monitoring of drug release by ratiometric $^{19}$F MRI.

Herein, we designed a pH-activated chemo-immunotherapy nanoplatform (PFZF-Dox NPs) with *in situ* monitoring drug

*State Key Laboratory of Chemical Resource Engineering, College of Chemistry, Beijing University of Chemical Technology, Beijing 100029, China. E-mail: lywang@mail.buct.edu.cn; guoc@mail.buct.edu.cn*

† Electronic supplementary information (ESI) available. See DOI: https://doi.org/10.1039/d4sc03643c

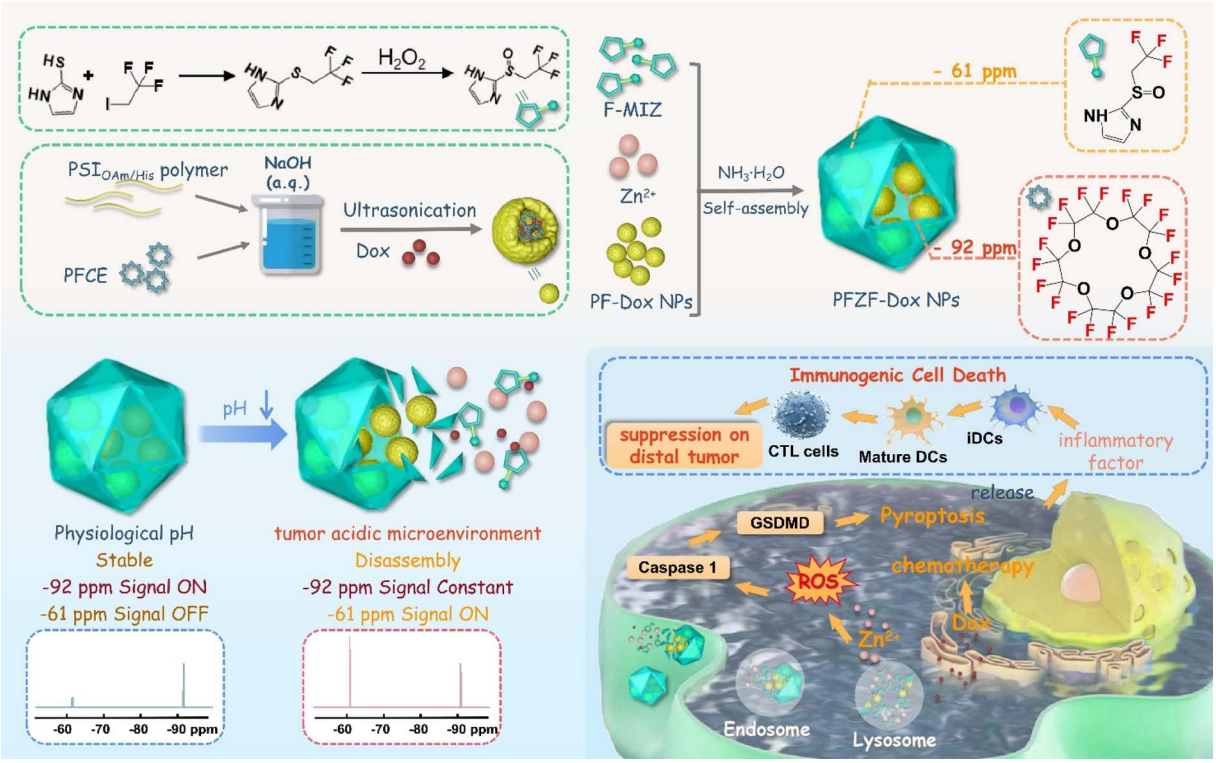


Scheme 1 Schematic illustration of the fabrication and properties of PFZF-Dox NPs (PF: PFCE nanodroplets; Z: $Zn^{2+}$; F: 2-((2,2,2-trifluoroethyl) sulfinyl)-1*H*-imidazole). PFZF-Dox NPs consist of small-sized perfluoro-15-crown-5-ether (PFCE) nanodroplets (PF-Dox NPs) coated with trifluoromethyl-containing metal–organic assemblies. After being taken up by the cells, PFZF-Dox NPs continuously released Dox and $Zn^{2+}$ into tumor cells, which evoked pyroptosis and chemotherapy. The released inflammatory factor cellular content would induce immunogenic cell death (ICD).

release capability by ratiometric $^{19}$F MRI (Scheme 1). In brief, we fabricated hydrophilic ultra-small (about 3 nm) perfluoro-15-crown-5-ether (PFCE) nanodroplets (termed PF-3 NPs) loaded with doxorubicin (Dox) using histamine (His) and oleylamine (OAm) modified poly(succinimide) (PSI). And then these nanodroplets were packaged in trifluoromethyl-containing metal–organic assemblies *via* coordination-driven self-assembly under basic conditions to get PFZF-Dox NPs (PF: PFCE nanodroplets; Z: $Zn^{2+}$; F: 2-((2,2,2-trifluoroethyl)sulfinyl)-1*H*-imidazole; Dox: doxorubicin). PFCE was chosen as the one color (chemical shift at −92 ppm) whose $^{19}$F NMR signal was kept constant, which serves as the internal reference signal. Additionally, trifluoromethyl (chemical shift at −61 ppm) in metal–organic assemblies was chosen as the other color for the nanoplatform. In a mild acidic microenvironment, the trifluoromethyl-containing metal–organic assemblies gradually decompose, causing the change of the $^{19}$F NMR signal at −61 ppm, as well as Dox release. This signal increases during assembly degradation, which serves as the response signal of Dox release. The ratiometric $^{19}$F MRI signal ($F_{-61ppm}/F_{-92ppm}$) was linear with pH value and independent of the concentrations of PFZF-Dox NPs. As a result, a linear correlation between the Dox release profile and ratiometric $^{19}$F MRI signal was established for quantitative detection *in vivo*. Furthermore, trifluoromethyl-containing metal–organic assemblies as a $Zn^{2+}$ releasing agent can intrinsically induce pyroptosis by a caspase-1/gasdermin D (GSDMD)-dependent pathway. Combinations of $Zn^{2+}$ evoked pyroptosis and chemotherapeutic Dox not only exhibited significant potential in cancer therapy but also induced the immunogenic cell death (ICD) of tumor cells, which provide new strategies and inspiration for imaging-guided cancer treatments with the capability of *in vivo* visualization of drug release.

## Results and discussion

### Preparation and characterization

PFZF-Dox NPs were synthesized *via* a two-step process, as illustrated in Scheme 1. First, PF-Dox NPs were prepared by co-encapsulating PFCE and Dox with a histamine (His) functionalized amphiphilic polymer ($PSI_{OAm/His}$). The $PSI_{OAm/His}$ with different amounts of His was prepared by aminolysis of the lactam ring on the poly(succinimide) (PSI) with His and oleylamine (OAm). Under optimized conditions, the contents of OAm and His were fixed at 30% of the succinimide units, respectively. Subsequently, PF NPs (PF-30 NPs, PF-5 NPs, and PF-3 NPs) with diameters of 30, 5 and 3 nm were synthesized by ultrasonic emulsification (Fig. S1–S4†). The PF-3 NPs were then chosen for subsequent experiments because the small nanoparticles showed superior penetration behavior.[38,39] It is notable that, if not otherwise specified, the PFZF was fabricated using PF-3 NPs in this work.

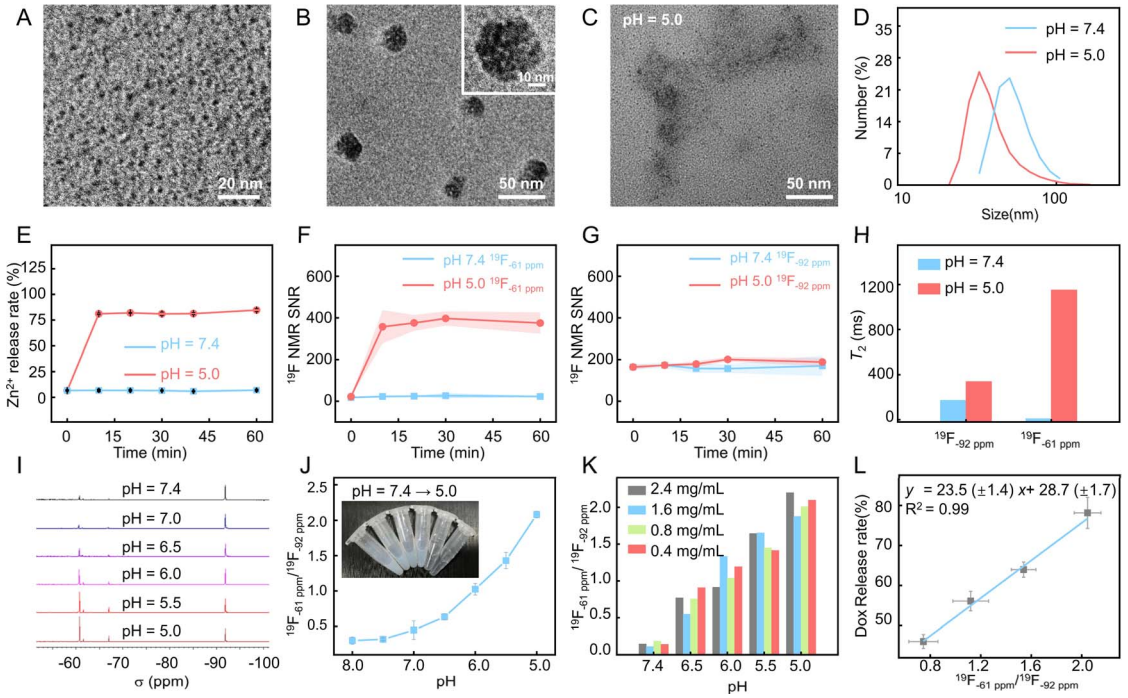


Fig. 1 (A) TEM image of PF NPs. (B) TEM image of PFZF-Dox NPs at pH 7.4. (C) TEM image of PFZF-Dox NPs at pH 5.0. (D) DLS size distribution of PFZF-Dox NPs at pH 7.4 and pH 5.0. (E) Cumulative release of $Zn^{2+}$ from PFZF-Dox NPs under different conditions along with time ($n = 3$). (F) $^{19}F$ NMR signal intensities at −61 ppm at pH 7.4 and 5.0 along with time ($n = 3$). (G) $^{19}F$ NMR signal intensities at −92 ppm at pH 7.4 and 5.0 along with time ($n = 3$). (H) $T_2$ relaxation time for $^{19}F$ NMR at −61 ppm and −92 ppm of PFZF NPs at pH 7.4 and 5.0. (I) $^{19}F$ NMR spectra of PFZF NPs at different pH. (J) The $^{19}F$ NMR signal intensities at −61 ppm/$^{19}F$ NMR signal intensities at −92 ppm ($^{19}F_{-61}/^{19}F_{-92}$) of PFZF NPs at different pH. Inset: The photograph of PFZF NPs under different pH conditions. (K) The $^{19}F_{-61}/^{19}F_{-92}$ signal ratio intensity of PFZF NPs at different pH. Measurements were performed at four different concentrations of PFZF-Dox NPs. (L) Correlation curve of the signal ratio intensity and Dox release percentage.

The transmission electron microscopy (TEM) image (Fig. 1A and S5†) indicated the successful construction of PF NPs with an average particle size of 3.0 ± 0.6 nm. Based on the coordination between the fluorinated imidazole group and $Zn^{2+}$, the PF NPs were further assembled into nanoplatforms. Compared to our previously used 4-trifluoromethyl imidazole,[40] the hydrophilicity of newly developed 2-((2,2,2-trifluoroethyl)sulfinyl)-1*H*-imidazole (Fig. S6–S9†) was greatly improved. After optimization of pH and $Zn^{2+}$ doses (Fig. S10 and S11†), spherical PFZF-Dox NPs (Fig. 1B) with a dynamic light scattering (DLS) size of 54 ± 14 nm (Fig. S12†) were successfully fabricated. The elements including C (41.9%), N (11.0%), O (30.3%), F (8.4%), and Zn (8.4%) on PFZF NPs were confirmed by X-ray photoelectron spectroscopy (XPS) (Fig. S13†).

### pH-activated drug release monitoring by ratiometric $^{19}F$ NMR

To verify the pH-responsive degradation and $Zn^{2+}$ ion release ability, the obtained PFZF-Dox NPs were dispersed into phosphate buffered saline (PBS) solutions with different pH values (7.4, 6.0, and 5.0), respectively. As shown in Fig. S14,† at pH 7.4, PFZF-Dox NPs maintained spherical nanoparticles without apparent degradation. In contrast, after being treated with an acidic buffer solution (pH 5.0) for 10 min, the PFZF-Dox NPs showed noticeable degradation, and no intact PFZF-Dox NPs could be observed (Fig. 1C), which was further confirmed by the decreased DLS sizes (Fig. 1D). As shown in Fig. 1E, the accumulated $Zn^{2+}$ ion release profile indicated that the release rate under acidic conditions reached 84% within 10 min, however, it displayed a negligible release over 60 min in a neutral environment. To verify the pH-responsive Dox release capability, the obtained PFZF-Dox NPs were dispersed in PBS solutions with pH values of 7.4 and 5.0. As shown in Fig. S15,† the accumulated Dox release profile indicated that the release rate under acidic conditions reached 72% within 10 minutes, whereas it exhibited minimal release over 60 minutes in a neutral environment.

As depicted in Scheme 1, The PFZF-Dox NPs displayed $^{19}F$ NMR peaks at −61 ppm and −92 ppm, belonging to trifluoromethyl in 2-((2,2,2-trifluoroethyl)sulfinyl)-1*H*-imidazole (F-MIZ) and PFCE in PF-Dox NPs, respectively. Under acidic conditions (pH 5.0), the $^{19}F$ NMR signal at −61 ppm was increased from 22 to 375 within 10 min (Fig. 1F). When exposed to a neutral environment (pH 7.4) even up to 60 minutes, the $^{19}F$ NMR signal at −61 ppm remains unchanged due to the mobility restriction of F-MIZ and thus attenuation of the $^{19}F$ NMR signal in the intact nanoplatform. Meanwhile, under both neutral (pH 7.4) and acidic (pH 5.0) conditions, the $^{19}F$ NMR signal at −92 ppm was relatively stable, which can be attributed to the highly hydrophobic and significantly lipophobic properties of PFCE ($^{19}F$ nuclei at −92 ppm) in PF NPs and it tends to segregate from the surrounding environment and exists as a droplet itself, resulting in its mobility unchanging with pH (Fig. 1G).

Apart from the signal intensity changes, the variation of the transverse ($T_2$) relaxation time of $^{19}$F nuclei at −92 ppm and −61 ppm was also checked (Fig. 1H). Notably, the $T_2$ values of $^{19}$F nuclei at −61 ppm increased under acidic conditions (pH 5.0), with a ∼121-fold increase from 9.5 ms to 1151.6 ms, which could be attributed to the degradation of PFZF NPs because the excellent mobility of the fluorine group is in favor of a long $T_2$ value and thus a high $^{19}$F NMR signal.[41] Fig. 1I shows the $^{19}$F NMR spectra of PFZF NPs under different pH conditions. With the pH decrease from 7.4 to 5.0 and the corresponding decomposition of the nanoplatform, the $^{19}$F NMR signal at −61 ppm increased step by step, which can be used for a pH-responsive signal. Meanwhile, the signal at −92 ppm remained stable, serving as the reference signal in the ratiometric $^{19}$F MRI monitoring of drug release.

The $^{19}F_{-61}/^{19}F_{-92}$ signal ratio gradually increased with the pH decrease, and the inset photographs (from colloid to solution) confirmed the decomposition of PFZF NPs under acidic conditions (Fig. 1J). As shown in Fig. 1K, the $^{19}F_{-61}/^{19}F_{-92}$ signal ratio was independent of the concentration of PFZF NPs but highly related to pH. Subsequently, we tested the potential of this ratiometric $^{19}$F MRI to monitor drug release. A linear relationship between cumulatively released Dox and the $^{19}F_{-61}/^{19}F_{-92}$ signal ratio was found (Fig. 1L, $y = 23.5\ (\pm 1.4)\ x + 28.7\ (\pm 1.7)$, $R^2 = 0.99$), indicating that the ratiometric signal intensity could be used for quantitative monitoring of the Dox release.

### Cell internalization and tumor penetration

Before the *in vivo* $^{19}$F MRI monitoring application, the cellular uptake efficiency of PFZF NPs was investigated using Nile red to monitor the location of the nanoplatforms. As shown in Fig. 2A and B, negligible red fluorescence was observed after 1.0 h incubation, while it increased significantly by prolonging the incubation time. The cellular uptake efficiency was also evaluated by $^{19}$F NMR, and a similar behavior was observed (Fig. 2C). Moreover, 3D tumor organoids were built to investigate the intratumoral penetration capabilities of nanoplatforms. Fluorescence images of tumor spheroids after incubation with PF-3 and PF-30 NPs are exhibited in Fig. S16,† implying superior penetration behavior of the small PF NPs. Another control sample coated with ZF was prepared using 30 nm-sized PF NPs, termed PF-30ZF NPs (Fig. S17†). The dynamic light scattering size of PF-30ZF NPs is 61 ± 18 nm (Fig. S18†). As shown in Fig. 2D and E, the stronger red fluorescence was observed in the interior of 3D multicellular tumor cell spheroids treated with PF-3ZF NPs (the size of PF NPs was 3 nm), in contrast to those treated with PF-30ZF NPs, where red emission was only observed at the borderline of those spheroids. This could be attributed to the better penetration ability of small-size PF NPs after the decomposition of the PFZF nanoplatform.

### Cytotoxicity and pyroptosis pathways

Cytotoxicity of PFZF NPs was further investigated in 4T1 cells. As shown in Fig. S19,† only 15% of cell viability was observed after incubation with PFZF-Dox NPs (150 μg mL$^{-1}$) for 24 h.

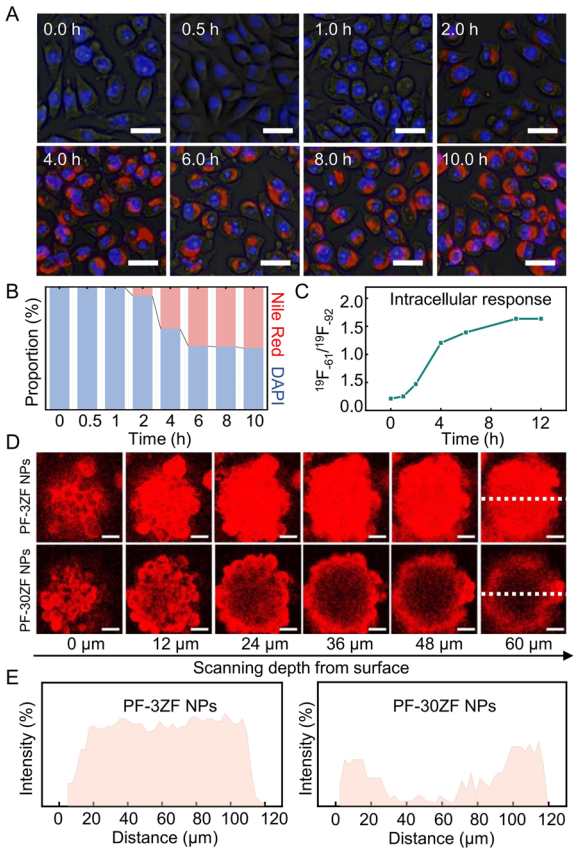


Fig. 2 (A) Confocal fluorescence images of 4T1 cells after incubation with PF-3ZF NPs. The scale bar is 20 μm. (B) Quantitative data from (A). (C) $^{19}$F NMR signal ratio of 4T1 cells treated with PFZF NPs along with time. (D) Confocal fluorescence images of 4T1 3D tumor spheroids after incubation with PF-3ZF and PF-30 ZF NPs (scale bar = 25 μm). (E) Quantitative analysis of red fluorescence intensities in different groups for line scanning of 3D tumor spheroids at a given depth.

Meanwhile, after incubation with PFZF NPs without Dox (150 μg mL$^{-1}$) for 24 h, the 4T1 cells maintained viability over 75%, implying that Dox mainly induced the cell toxicity. However, compared with PF-Dox NPs, the PFZF-Dox NPs with a consistent molar concentration of doxorubicin (Dox) showed significantly enhanced cytotoxicity (Fig. S20†), which may be attributed to the synergism of Dox and $Zn^{2+}$ released from PFZF NPs. Then, 2′,7′-dichlorodihydro fluorescein diacetate (DCFH-DA) was used to evaluate the intracellular oxidative stress (Fig. 3A top and S21†). The groups treated with PFZF NPs (II) and PFZF-Dox NPs (V) revealed an increase in ROS generation when compared with the PBS (I), free Dox (III) and PF-Dox NP group, which might have resulted from sudden surges in $Zn^{2+}$ ions and homeostasis disequilibrium. Similar to the above results, confocal laser scanning microscopy (CLSM) images of 4T1 cells with different treatments indicated significant changes in mitochondrial membrane depolarization, verified through fluorescence staining with a mitochondrial membrane potential probe (JC-1). The groups treated with PFZF-Dox NPs (Fig. 3A bottom and S22†) revealed a decrease in the red-to-green emission ratio compared with the PBS group, implying the stronger depolarization of the

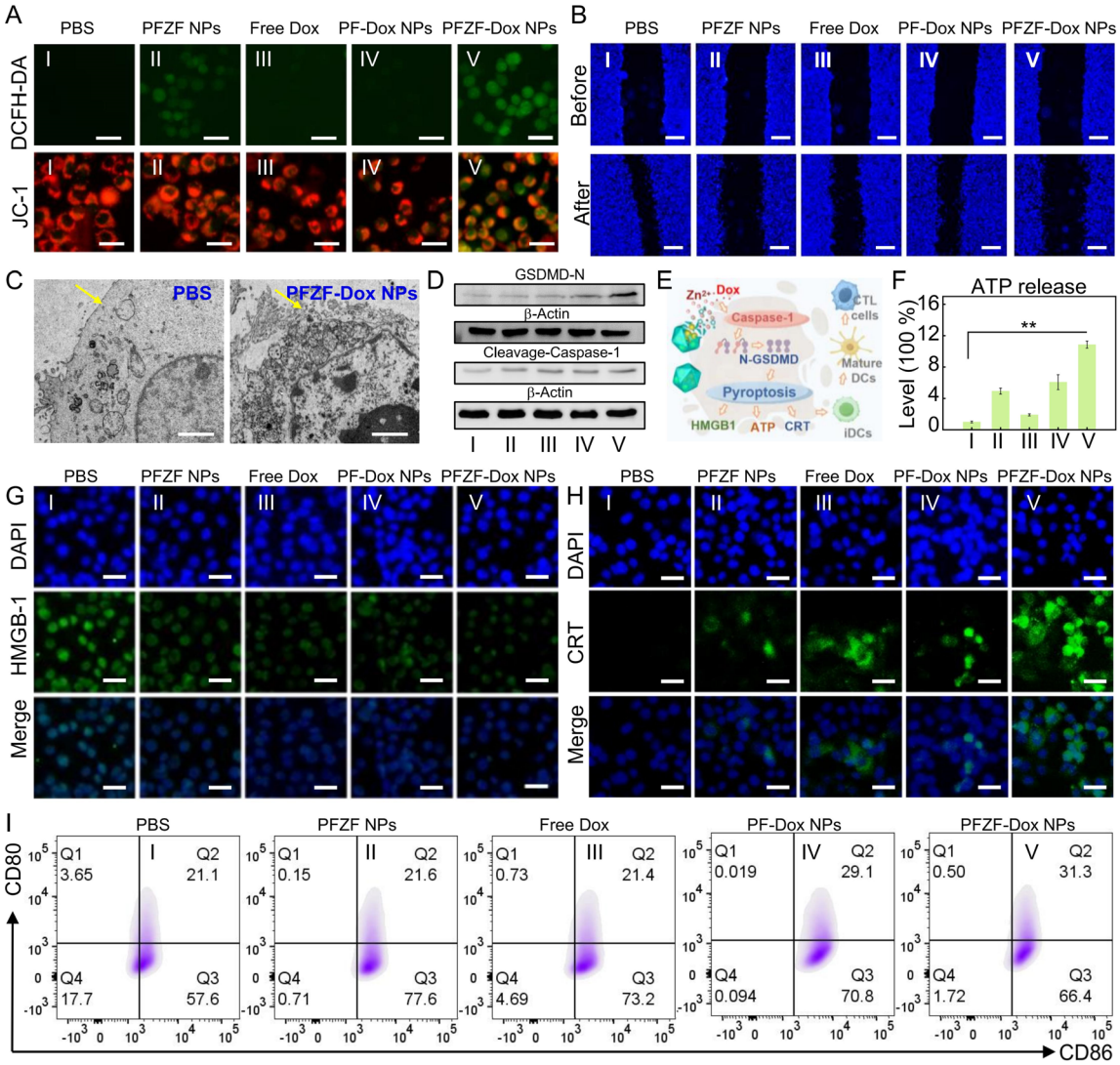


Fig. 3 (A) CLSM fluorescence images of 4T1 cells after different formulations, followed by staining with DCFH-DA (ROS generation indicator) and JC-1, respectively. The scale bar represents 20 μm. (B) Cell migration assay of 4T1 cells after different formulations. The scale bar represents 100 μm. (C) Bio-TEM images. The scale bar represents 2 μm. (D) Western blot analysis of Caspase-1 and GSDMD proteins after different formulations. (E) The scheme of PFZF-Dox NPs promoting the ICD. (F) Extracellular ATP levels from 4T1 cells after different treatments for 12 h ($n = 3$). (G and H) Immunofluorescence detection of HMGB-1 (G) and CRT (H) expressed. Cells as observed by CLSM (scale bar = 20 μm). (I) Flow cytometric analysis of DC maturation after 24 h coculture with ICD cancer cells generated through different treatments. (I) PBS; (II) PFZF NPs; (III) free Dox; (IV) PF-Dox NPs; (V) PFZF-Dox NPs.

mitochondrial membranes. Fig. 3B and S23† show the cell migration assay of 4T1 cells after different formulations, implying that PFZF-Dox NPs can inhibit cell migration, which may be mainly attributed to the growth hindrance of high concentration of zinc.[42]

PFZF-Dox NP mediated pyroptosis leads to apparent mitochondrial destruction with obvious swelling and blebbing (Fig. 3C). Moreover, previous studies[43,44] have established that cleavage of gasdermin D (GSDMD) by inflammatory caspases is considered a vital step in initiating pyroptosis, leading to the release of the N-terminal domain of GSDMD (GSDMD-N). This domain binds to membrane phospholipids and forms pores on cellular membranes, resulting in cell rupture. Therefore, we investigated the expression of crucial pyroptosis proteins. As shown in Fig. 3D, PFZF NPs gave rise to the highest expression of cleaved caspase-1 and GSDMD, clearly indicating that they may induce 4T1 cell pyroptosis through the caspase-1/GSDMD pathway.

### Induce immunogenic cell death *in vitro*

Pyroptosis further promotes massive amounts of inflammatory molecule release, ultimately achieving antitumor immune activation. During immunogenic cell death (ICD), tumor cells release DAMPs, including calreticulin (CRT), adenosine triphosphatase (ATP), and high mobility group box-1 (HMGB-1) (Fig. 3E). To investigate immune activation, hallmark markers of immunogenic cell death were evaluated. As depicted in

Fig. 3F, among all the groups, the PFZF-Dox NP treated group (V) exhibited the most significant release of extracellular ATP, while the PFZF NP group (II) demonstrated moderate ATP release. The $Zn^{2+}$ substantially enhanced oxidative stress to induce immunogenic cell death, as evidenced by the lower retention of HMGB-1 (Fig. 3G and S24†) in the cell nucleus and the highest expression levels of CRT (Fig. 3H and S25†), and thus significant ICD occurred.

Furthermore, the degree of DC maturation was assessed by culturing 4T1 cells under different treatments and subsequently co-incubating them with DCs using a transwell system. DCs in the bottom wells were collected and analyzed using flow cytometry to examine the expression of co-stimulatory molecules CD80 and CD86, which serve as markers of DC maturation (Fig. 3I). Compared to the other groups, treatment with PFZF-Dox NPs significantly elevated the levels of CD80 and CD86, suggesting that PFZF-Dox NP treatment can stimulate anti-tumor immune responses by promoting DC maturation.

### Visualization of Dox release by ratiometric $^{19}$F MRI

Next, the Dox release percentage of PFZF-Dox NPs was investigated by ratiometric $^{19}$F MRI in solution. MRI images of PFZF-Dox NPs were acquired using the appropriate radio frequency (RF) excitation pulse frequency with a bandwidth of 5000 Hz (~18 ppm) to cover the resonance frequencies. For proof-of-concept, PFZF-Dox NPs were dispersed in pH = 5.0 buffer solution to simulate the intracellular environment pH. $^{19}$F MRI images of PFZF-Dox NPs suspension under pH 5.0 along with time are shown in Fig. S26.† The ratiometric $^{19}$F MRI signal change corresponded with the Dox release rate across the different time points of the release process, which reached a plateau at 20 min. Next, PFZF-Dox NPs were dispersed in buffer at different pH values and then incubated at 37 °C for 20 min before measuring the $^{19}$F MRI signal. Fig. 4A shows an increasing $^{19}$F MRI signal at −61 ppm (red channel) and a constant $^{19}$F MRI signal at −92 ppm (blue channel), indicating the strong ratiometric $^{19}$F MRI response toward Dox released at different pH values. Significantly, a good linear relationship (Fig. 4D, $y = 41.9\ (\pm 0.8)\ x - 7.1\ (\pm 0.5)$, $R^2 = 0.99$) was observed between the Dox release profile (Fig. 4C) and the $^{19}F_{-61}/^{19}F_{-92}$ ratios (Fig. 4B), suggesting that PFZF-Dox NPs could effectively self-monitor the Dox release through the simultaneous output of ratiometric $^{19}$F MRI signals.

Encouraged by the promising *in vitro* performance of ratiometric $^{19}$F MRI observed in the PFZF-Dox NPs, we explored the feasibility of utilizing these NPs for stimuli-responsive tumor imaging. The PFZF-Dox NPs were intratumorally injected at the tumor site in the tumor-bearing mouse and the corresponding site of normal tissue in the healthy mouse, respectively (Fig. 4E). Due to the complexity of *in vivo* environments, the $^{19}$F NMR peak displayed varying degrees of broadening and shifting at different

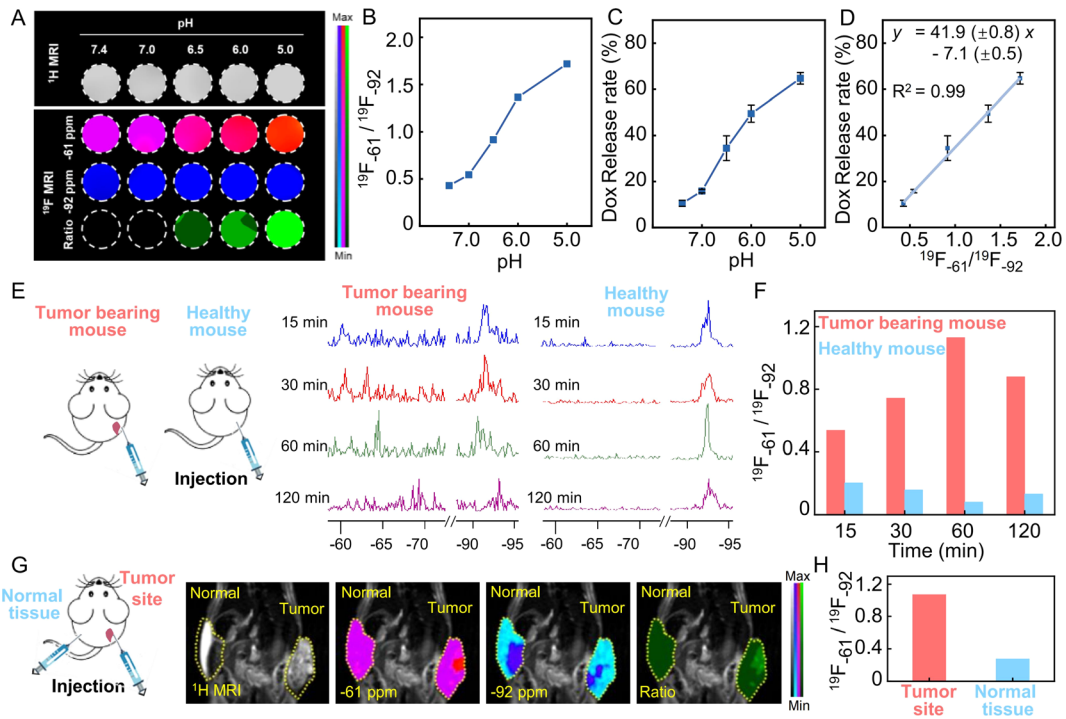


Fig. 4 (A) $^{1}$H MRI and $^{19}$F MRI images of PFZF NP suspension at different pH values. RF excitation pulse at −61 ppm (red channel) and −92 ppm (blue channel). (B) The plot of the $^{19}$F MRI intensity ratio ($^{19}F_{-61}/^{19}F_{-92}$) of PFZF-Dox NPs at different pH. (C) The plot of the Dox release percentage of PFZF-Dox NPs at different pH. Data are shown as the mean ± SD ($n = 3$). (D) The correlation fitting curve between the Dox release percentage and the ratiometric signal ($^{19}F_{-61}/^{19}F_{-92}$). Data are shown as the mean ± SD ($n = 3$). (E) $^{19}$F NMR of healthy and tumor-bearing mice treated with PFZF-Dox NPs (i.t.) at different times. (F) Corresponding quantitative data of the $^{19}$F NMR intensity ratio ($^{19}F_{-61}/^{19}F_{-92}$) treated with PFZF-Dox NPs (i.t.) at different time points. (G) $^{19}$F MRI of 4T1 tumor-bearing mice at 60 min post-injection. The same dosages of PFZF NPs were injected at the tumor site and normal tissue, respectively. (H) Quantitative data of $^{19}F_{-61}/^{19}F_{-92}$ obtained from (G).

time points. Therefore, monitoring the release status of Dox *in vivo* was challenging using a single $^{19}$F signal change. In order to overcome this issue, a ratiometric method was proposed. As shown in Fig. 4F, the ratiometric signals in the tumor-bearing mice were higher than those in the healthy mice at 15 minute time points following the administration of PFZF-Dox NPs. Afterward, the ratiometric signal of the tumor-bearing mouse increased obviously at 60 min and gradually decayed at 120 min.

Furthermore, the PFZF NPs were injected at the tumor site and subcutaneously in the normal tissue of the same mouse. We counted the $^{19}$F MRI intensity in tumor and normal tissue after 60 min post-injection (Fig. 4G), as well as calculated the ratios of the $^{19}$F MRI intensity of the two channels (−61 ppm and −92 ppm). As expected, a remarkable ratiometric $^{19}$F MRI signal was observed at the tumor site (Fig. 4H), whereas a negligible ratiometric $^{19}$F MRI signal was acquired in normal tissue, suggesting that the PFZF-Dox NPs were selectively activated at the tumor site. By employing quantitative relationships (Fig. 4D), it is possible to calculate the average percentage of Dox released in normal tissues to be 4%, whereas the average percentage of Dox released in tumor tissues is 38%. Additionally, we observe that the highest intensities in the images at

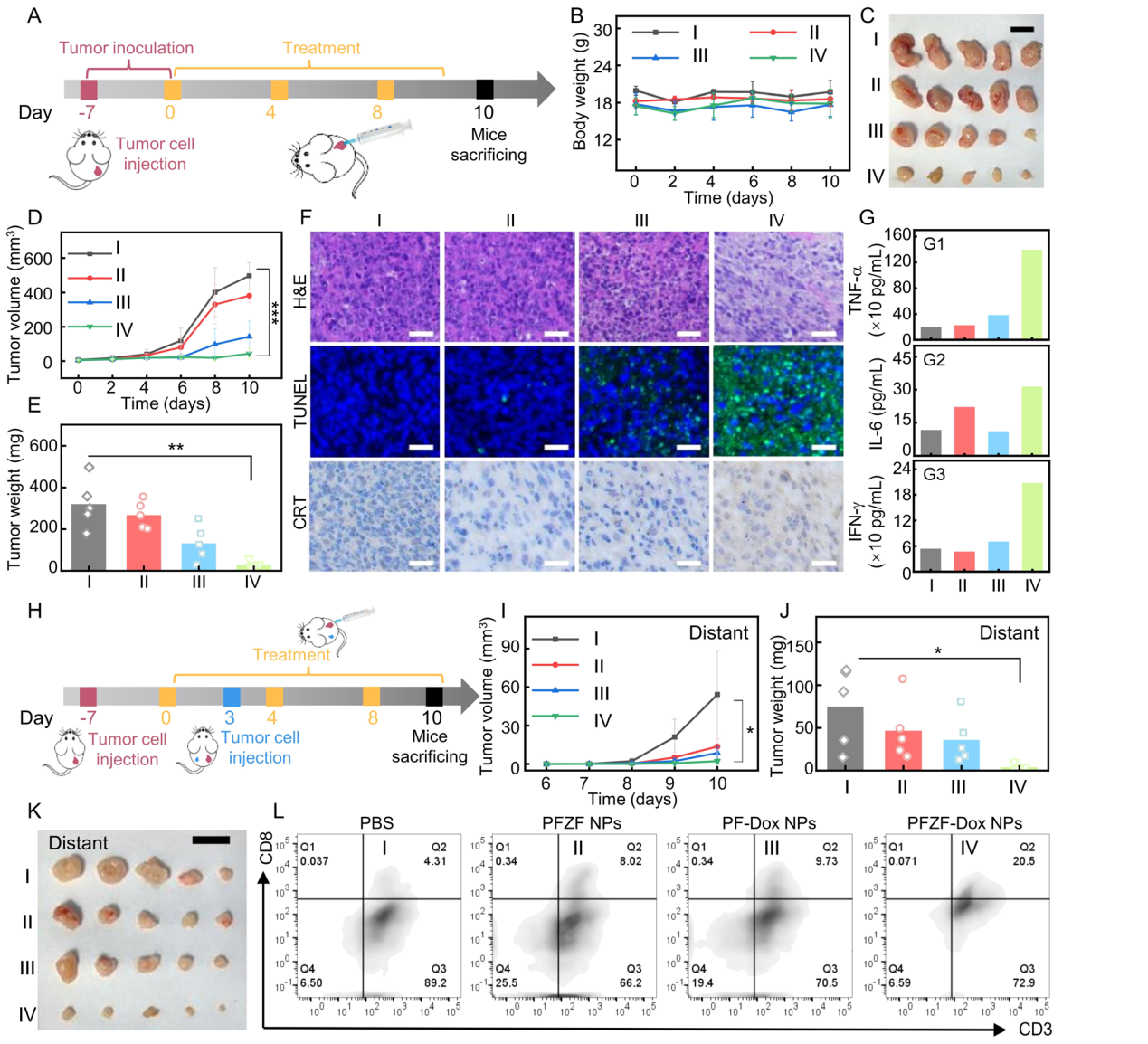


Fig. 5 *In vivo* antitumor efficacy of different administrations for 4T1 tumor-bearing Balb/c mice. (A) Schematic illustration of the administration design. (B) Body weight changes for mice within ten days. Data are shown as the mean ± SD ($n = 5$). (C) The photograph of tumor excision. The scale bar is 1.0 cm. (D) Tumor volume curves and (E) tumor weight of 4T1 tumor-bearing Balb/c mice after intravenous administrations. Data are shown as the mean ± SD ($n = 5$); *$p < 0.05$, **$p < 0.01$, ***$p < 0.001$, compared to the PBS group. (F) H&E, TUNEL, and CRT staining of tumor sections after different treatments. The scale bar is 20 μm. (G) Cytokine TNF-α (G1), IL-6 (G2), and INF-γ (G3) levels in peripheral blood serum after different treatment. (H) Schematic illustration of the treatment of distant tumors. (I) Tumor volume curves, (J) tumor weight, and (K) tumor excision photograph of 4T1 tumor-bearing Balb/c mice after intravenous administrations. The scale bar is 1.0 cm. Data are shown as the mean ± SD ($n = 5$); *$p < 0.05$, compared to the PBS group. (L) Flow cytometric analysis of the populations of CD8+ T cells. (I) PBS; (II) PFZF NPs; (III) PF-Dox NPs; and (IV) PFZF-Dox NPs.

−61 ppm and −92 ppm come from different anatomical locations. A possible explanation is that the released 2-((2,2,2-trifluoroethyl) sulfinyl)-1*H*-imidazole (chemical shift at −61 ppm) and PFCE (chemical shift at −92 ppm) accumulated in a different location.

### Antitumor effect evaluation *in vivo*

Considering the excellent *in vitro* anti-cancer activity and *in vivo* imaging performance of PFZF-Dox NPs, we further tested their *in vivo* cancer inhibition effect. Tumor-bearing mice were divided into four groups: (I) PBS; (II) PFZF NPs; (III) PF-Dox NPs; and (IV) PFZF-Dox NPs, which were treated with three peritumoral injections of different administrations (Fig. 5A). Moreover, we performed the $^{19}F$ MRI at different time points after peritumoral injections of PFZF-Dox NPs (Fig. S27†), and the ratiometric $^{19}F$ MRI signal ($^{19}F_{-61}/^{19}F_{-92}$) reached peak values at 9 h. At 10 days after tumor inoculation, there were no apparent changes in body weight, which suggests that the nanomaterials displayed good biocompatibility (Fig. 5B). Such treatment did not cause any toxicity to major organs such as the heart, liver, lung, and kidney, as demonstrated by the results of H&E staining (Fig. S28†), which further supported the biosafety of the as-prepared nanoplatforms. The tumor growth state depicted in Fig. 5C–E revealed that PFZF-Dox NP treatment resulted in a significant decrease in tumor volume, demonstrating a pronounced antitumor effect compared to the PBS group. Furthermore, the PF-Dox NP (III) group (without $Zn^{2+}$) displayed a secondary antitumor effect with a noticeable reduction in tumor growth. This phenomenon could be attributed to the loaded Dox.

Then, we investigated the impact of PFZF-Dox NPs on tumor growth suppression using Hematoxylin and Eosin (H&E) and Terminal Deoxynucleotidyl Transferase mediated dUTP Nick End Labeling (TUNEL) staining. Fig. 5F demonstrates that a substantial portion of cancer cells exhibited extensive necrosis and acellular regions following treatment with PFZF-Dox NPs. Furthermore, the TUNEL apoptosis assay indicated a higher occurrence of cellular apoptosis in the PFZF-Dox NP group. As shown in Fig. 5G, we investigated the *in vivo* immunostimulation in Balb/c mice with 4T1 tumors following various administrations. Tumor-bearing mice receiving PFZF-Dox NPs exhibited the highest levels of TNF-α, IL-6, and INF-γ in their peripheral blood serum on day ten post-injection, surpassing the levels observed in other groups. This increase was 2–3-fold higher than that observed in the PBS group. Increased CRT exposure was also visualized in 4T1 tumors from CRT staining (Fig. 5F). These results suggested that PFZF-Dox NPs triggered a strong release of ICD-associated DAMPs by combining Dox and $Zn^{2+}$ evoked pyroptosis.

To evaluate the antitumor immunity against tumor metastasis, we also conducted experiments in which 4T1 cells were subcutaneously inoculated into both flanks of the mouse dorsum, but nanoplatforms were only injected on the right flank (Fig. 5H). The growth of the distant tumor (left flank) was monitored on post-injection days 3, 4, 5, 6, and 7. Compared to control animals (Group I: PBS and Group II: PFZF NPs without Dox; Group III: PF-Dox NPs without $Zn^{2+}$), we found that local tumor recurrence on the left flank was significantly inhibited by PFZF-Dox NPs (Fig. 5I–K). Consistent with these results, the higher infiltration of CD8+ T cells was observed in the distant tumor of mice treated with PFZF-Dox NPs (Fig. 5L), leading to decreased tumor size compared to the control groups. Therefore, PFZF-Dox NPs can protect against the recurrence of distant tumors. Notably, PFZF NPs (without Dox) also delayed tumor growth, probably because these NPs could deliver $Zn^{2+}$ into tumor cells, which evoked pyroptosis and improved the immune response. Taken together, PFZF-Dox NPs demonstrated great potential in cancer therapy.

## Conclusions

In summary, we have successfully developed a multifunctional theranostic nanoplatform termed PFZF-Dox NPs. This nanoplatform can self-report the release of Dox in real-time through the ratiometric $^{19}F$ MRI signal. Notably, there is a consistent correlation between the ratiometric $^{19}F$ MRI signals ($^{19}F_{-61}/^{19}F_{-92}$) and the release rate of loaded Dox, regardless of the concentration of PFZF-Dox NPs. Based on this, the released Dox was successfully quantified *in vivo* through ratiometric $^{19}F$-MRI. Moreover, this nanoplatform presented a good tumor microenvironment-activated drug release performance, which would effectively minimize side effects. By combining chemotherapy with $Zn^{2+}$-induced pyroptosis, a remarkable therapeutic efficacy was achieved, substantially reducing the primary tumor and inhibiting distal tumor growth. This nanoplatform presented a promising approach for real-time imaging and quantifying *in vivo* drug release during cancer treatment.

## Data availability

The data supporting this article have been included as part of the ESI.† Any additional information required to reanalyze the data reported in this paper is available from the contact upon request.

## Author contributions

L. Wang and C. Guo designed and conceived the research. F. Liu prepared and measured all samples and analyzed the data. X. Li and Y. Li helped with preparing the materials and analyzing the data. C. Guo., S. Xu, and L. Wang supported this research. C. Guo and F. Liu wrote this paper with input from other authors. All the authors discussed the results and commented on the manuscript.

## Conflicts of interest

There are no conflicts to declare.

## Acknowledgements

This research was partly supported by the National Natural Science Foundation of China (22334002, 22322402, and

 

22306010), Beijing Municipal Natural Science Foundation (Z231100002723006), and the Fundamental Research Funds for the Central Universities (JD2308 and XK2023-19). All experiments involving animals were performed in accordance with the guidelines of the Institutional Animal Care and Use Committee (IACUC) of the China–Japan Friendship Hospital and Beijing University of Chemical Technology.

## Notes and references

1 S. E. Boyken, M. A. Benhaim, F. Busch, M. Jia, M. J. Bick, H. Choi, J. C. Klima, Z. Chen, C. Walkey, A. Mileant, A. Sahasrabuddhe, K. Y. Wei, E. A. Hodge, S. Byron, A. Quijano-Rubio, B. Sankaran, N. P. King, J. Lippincott-Schwartz, V. H. Wysocki, K. K. Lee and D. Baker, De novo design of tunable, pH-driven conformational changes, *Science*, 2019, **364**, 658–664.

2 N. J. Hunt, G. P. Lockwood, S. J. Heffernan, J. Daymond, M. Ngu, R. K. Narayanan, L. J. Westwood, B. Mohanty, L. Esser, C. C. Williams, Z. Kuncic, P. A. G. McCourt, D. G. Le Couteur and V. C. Cogger, Oral nanotherapeutic formulation of insulin with reduced episodes of hypoglycaemia, *Nat. Nanotechnol.*, 2024, **19**, 534–544.

3 J. Shen, M. Ma, M. Shafiq, H. Yu, Z. Lan and H. Chen, Microfluidics-Assisted Engineering of pH/Enzyme Dual-Activatable ZIF@Polymer Nanosystem for Co-Delivery of Proteins and Chemotherapeutics with Enhanced Deep-Tumor Penetration, *Angew. Chem., Int. Ed.*, 2022, **61**, e202113703.

4 M. A. English, L. R. Soenksen, R. V. Gayet, H. de Puig, N. M. Angenent-Mari, A. S. Mao, P. Q. Nguyen and J. J. Collins, Programmable CRISPR-responsive smart materials, *Science*, 2019, **365**, 780–785.

5 X. Wen, R. Zhang, Y. Hu, L. Wu, H. Bai, D. Song, Y. Wang, R. An, J. Weng, S. Zhang, R. Wang, L. Qiu, J. Lin, G. Gao, H. Liu, Z. Guo and D. Ye, Controlled sequential in situ self-assembly and disassembly of a fluorogenic cisplatin prodrug for cancer theranostics, *Nat. Commun.*, 2023, **14**, 800.

6 M. Wensien, F. R. von Pappenheim, L.-M. Funk, P. Kloskowski, U. Curth, U. Diederichsen, J. Uranga, J. Ye, P. Fang, K.-T. Pan, H. Urlaub, R. A. Mata, V. Sautner and K. Tittmann, A lysine–cysteine redox switch with an NOS bridge regulates enzyme function, *Nature*, 2021, **593**, 460–464.

7 Z. Zhao, A. Ukidve, J. Kim and S. Mitragotri, Targeting Strategies for Tissue-Specific Drug Delivery, *Cell*, 2020, **181**, 151–167.

8 M. J. Baek, D. T. Nguyen, D. Kim, S. Y. Yoo, S. M. Lee, J. Y. Lee and D. D. Kim, Tailoring renal-clearable zwitterionic cyclodextrin for colorectal cancer-selective drug delivery, *Nat. Nanotechnol.*, 2023, **18**, 945–956.

9 M. M. Rahman, J. Wang, G. Wang, Z. Su, Y. Li, Y. Chen, J. Meng, Y. Yao, L. Wang, S. Wilkens, J. Tan, J. Luo, T. Zhang, C. Zhu, S. H. Cho, L. Wang, L. P. Lee and Y. Wan, Chimeric nanobody-decorated liposomes by self-assembly, *Nat. Nanotechnol.*, 2024, **19**, 818–824.

10 X. Li, M. Bottini, L. Zhang, S. Zhang, J. Chen, T. Zhang, L. Liu, N. Rosato, X. Ma, X. Shi, Y. Wu, W. Guo and X. Liang, Core–Satellite Nanomedicines for in Vivo Real-Time Monitoring of Enzyme-Activatable Drug Release by Fluorescence and Photoacoustic Dual-Modal Imaging, *ACS Nano*, 2019, **13**, 176–186.

11 D. B. Cheng, X. H. Zhang, S. Y. Chen, X. X. Xu, H. Wang and Z. Y. Qiao, Intracellular Self-Immolative Polyprodrug with Near-Infrared Light Guided Accumulation and in Vivo Visualization of Drug Release, *Adv. Mater.*, 2022, **34**, 2109528.

12 R. M. Borum, C. Moore, Y. Mantri, M. Xu and J. V. Jokerst, Supramolecular Loading of DNA Hydrogels with Dye–Drug Conjugates for Real-Time Photoacoustic Monitoring of Chemotherapy, *Adv. Sci.*, 2023, **10**, 2204330.

13 S. Lacerda, A. Delalande, S. V. Eliseeva, A. Pallier, C. S. Bonnet, F. Szeremeta, S. Même, C. Pichon, S. Petoud and É. Tóth, Doxorubicin-Sensitized Luminescence of NIR-Emitting Ytterbium Liposomes: Towards Direct Monitoring of Drug Release, *Angew. Chem., Int. Ed.*, 2021, **60**, 23574–23577.

14 S. Wang, Z. Zhou, Z. Wang, Y. Liu, O. Jacobson, Z. Shen, X. Fu, Z.-Y. Chen and X. Chen, Gadolinium Metallofullerene-Based Activatable Contrast Agent for Tumor Signal Amplification and Monitoring of Drug Release, *Small*, 2019, **15**, 1900691.

15 B. Li, W. Wang, L. Zhao, Y. Wu, X. Li, D. Yan, Q. Gao, Y. Yan, J. Zhang, Y. Feng, J. Zheng, B. Shu, J. Wang, H. Wang, L. He, Y. Zhang, M. Pan, D. Wang, B. Z. Tang and Y. Liao, Photothermal therapy of tuberculosis using targeting pre-activated macrophage membrane-coated nanoparticles, *Nat. Nanotechnol.*, 2024, **19**, 834–845.

16 M. Brady, V. I. Shchepetkina, I. González-Recio, M. L. Martínez-Chantar and D. Buccella, Ratiometric Fluorescent Sensors Illuminate Cellular Magnesium Imbalance in a Model of Acetaminophen-Induced Liver Injury, *J. Am. Chem. Soc.*, 2023, **145**, 21841–21850.

17 Y. Liu, L. Teng, Y. Lyu, G. Song, X.-B. Zhang and W. Tan, Ratiometric afterglow luminescent nanoplatform enables reliable quantification and molecular imaging, *Nat. Commun.*, 2022, **13**, 2216.

18 Z. Fang, C. Wang, J. Yang, Z. Song, C. Xie, Y. Ji, Z. Wang, X. Du, Q. Zheng, C. Chen, Z. Hu and Y. Zhong, Oxyhaemoglobin saturation NIR-IIb imaging for assessing cancer metabolism and predicting the response to immunotherapy, *Nat. Nanotechnol.*, 2023, **19**, 124–130.

19 Z. Jiang, C. Zhang, X. Wang, Z. Ling, Y. Chen, Z. Guo and Z. Liu, A Small-Molecule Ratiometric Photoacoustic Probe for the High-Spatiotemporal-Resolution Imaging of Copper(II) Dynamics in the Mouse Brain, *Angew. Chem., Int. Ed.*, 2024, **63**, e202318340.

20 D. Tang, H. Zhou, M. Cui, G. Liang, H. Zhang and H. Xiao, NIR-II Light Accelerated Prodrug Reduction of Pt(IV)-Incorporating Pseudo Semiconducting Polymers for Robust Degradation and Maximized Photothermal/Chemo-Immunotherapy, *Adv. Mater.*, 2023, **35**, 2300048.

21 F. Wang, Y. Zhong, O. Bruns, Y. Liang and H. Dai, In vivo NIR-II fluorescence imaging for biology and medicine, *Nat. Photonics*, 2024, **18**, 535–547.

22 S. Z. Chen, L. Xiao, Y. Li, M. S. Qiu, Y. P. Yuan, R. Zhou, C. G. Li, L. Zhang, Z. X. Jiang, M. Liu and X. Zhou, In Vivo Nitroreductase Imaging via Fluorescence and Chemical Shift Dependent $^{19}$F NMR, *Angew. Chem., Int. Ed.*, 2022, **61**, e202213495.

23 H. Zhu, X. Yin, Y. Zhou, S. Y. Xu, T. D. James and L. Y. Wang, Nanoplatforms with synergistic redox cycles and rich defects for activatable image-guided tumor-specific therapy, *Chem*, 2022, **8**, 2498–2513.

24 R. T. Kadakia, R. T. Ryan, D. J. Cooke and E. L. Que, An Fe complex for $^{19}$F magnetic resonance-based reversible redox sensing and multicolor imaging, *Chem. Sci.*, 2023, **14**, 5099–5105.

25 L. L. Lock, Y. Li, X. Mao, H. Chen, V. Staedtke, R. Bai, W. Ma, R. Lin, Y. Li, G. Liu and H. Cui, One-Component Supramolecular Filament Hydrogels as Theranostic Label-Free Magnetic Resonance Imaging Agents, *ACS Nano*, 2017, **11**, 797–805.

26 X. Zhu, R. Tang, S. Wang, X. Chen, J. Hu, C. Lei, Y. Huang, H. Wang, Z. Nie and S. Yao, Protein@Inorganic Nanodumpling System for High-Loading Protein Delivery with Activatable Fluorescence and Magnetic Resonance Bimodal Imaging Capabilities, *ACS Nano*, 2020, **14**, 2172–2182.

27 R. Yue, C. Zhang, L. Xu, Y. Wang, G. Guan, L. Lei, X. Zhang and G. Song, Dual key co-activated nanoplatform for switchable MRI monitoring accurate ferroptosis-based synergistic therapy, *Chem*, 2022, **8**, 1956–1981.

28 S. Langereis, J. Keupp, J. L. J. van Velthoven, I. H. C. de Roos, D. Burdinski, J. A. Pikkemaat and H. Grüll, A Temperature-Sensitive Liposomal $^{1}$H CEST and $^{19}$F Contrast Agent for MR Image-Guided Drug Delivery, *J. Am. Chem. Soc.*, 2009, **131**, 1380–1381.

29 G. Guan, C. Zhang, H. Liu, Y. Wang, Z. Dong, C. Lu, B. Nan, R. Yue, X. Yin, X.-B. Zhang and G. Song, Ternary Alloy PtWMn as a Mn Nanoreservoir for High-Field MRI Monitoring and Highly Selective Ferroptosis Therapy, *Angew. Chem., Int. Ed.*, 2022, **61**, e202117229.

30 C. Guo, Q. Q. Nie, S. Y. Xu and L. Y. Wang, $^{19}$F-Grafted Fluorescent Carbonized Polymer Dots for Dual-Mode Imaging, *Anal. Chem.*, 2021, **93**, 13880–13885.

31 C. Guo, Y. Yan, S. Y. Xu and L. Y. Wang, In Situ Fabrication of Nanoprobes for $^{19}$F Magnetic Resonance and Photoacoustic Imaging-Guided Tumor Therapy, *Anal. Chem.*, 2022, **94**, 5317–5324.

32 C. Guo, Y. Y. Zhang, Y. W. Li, S. Y. Xu and L. Y. Wang, $^{19}$F MRI nanoprobes for the turn-on detection of phospholipase A2 with a low background, *Anal. Chem.*, 2019, **91**, 8147–8153.

33 F. Liu, C. Guo, X. Li, Y. Li, S. Y. Xu, T. D. James and L. Y. Wang, A versatile nano-transformer for efficient localization-specific imaging and synergistic therapy of bladder cancer, *Nano Today*, 2024, **54**, 102116.

34 C. Sire, V. Meneyrol, N. Saffon-Merceron, E. Terreno, F. Garello, L. Tei, E. Jestin, R. Tripier and T. Troadec, A versatile fluorinated azamacrocyclic chelator enabling $^{18}$F PET or $^{19}$F MRI: a first step towards new multimodal and smart contrast agents, *Chem. Sci.*, 2024, **15**, 13550–13557.

35 M. J. Afshari, X. Cheng, G. Duan, R. Duan, S. Wu, J. Zeng, Z. Gu and M. Gao, Vision for Ratiometric Nanoprobes: In Vivo Noninvasive Visualization and Readout of Physiological Hallmarks, *ACS Nano*, 2023, **17**, 7109–7134.

36 X. Huang, J. Song, B. C. Yung, X. Huang, Y. Xiong and X. Chen, Ratiometric optical nanoprobes enable accurate molecular detection and imaging, *Chem. Soc. Rev.*, 2018, **47**, 2873–2920.

37 N. Genicio, M. Bañobre-López, O. Gröhn and J. Gallo, Ratiometric magnetic resonance imaging: Contrast agent design towards better specificity and quantification, *Coord. Chem. Rev.*, 2021, **447**, 214150.

38 J. Wang, Z. Fang, C. Zhao, Z. Sun, S. Gao, B. Zhang, D. Qiu, M. Yang, F. Sheng, S. Gao and Y. Hou, Intelligent Size-Switchable Iron Carbide-Based Nanocapsules with Cascade Delivery Capacity for Hyperthermia-Enhanced Deep Tumor Ferroptosis, *Adv. Mater.*, 2023, **36**, 2307006.

39 W. Chen, W. Wang, Z. Xie, F. Centurion, B. Sun, D. J. Paterson, S. C.-H. Tsao, D. Chu, Y. Shen, G. Mao and Z. Gu, Size-Dependent Penetration of Nanoparticles in Tumor Spheroids: A Multidimensional and Quantitative Study of Transcellular and Paracellular Pathways, *Small*, 2023, **20**, 2304693.

40 C. Guo, S. Y. Xu, A. Arshad and L. Y. Wang, A pH-responsive nanoprobe for turn-on $^{19}$F magnetic resonance imaging, *Chem. Commun.*, 2018, **54**, 9853–9856.

41 S. Kaufman, J. M. Steim and J. H. Gibbs, Nuclear Relaxation in Phospholipids and Biological Membranes, *Nature*, 1970, **225**, 743–744.

42 Q. Xin, H. Zhang, Q. Liu, Z. Dong, H. Xiang and J. R. Gong, Extracellular Biocoordinated Zinc Nanofibers Inhibit Malignant Characteristics of Cancer Cell, *Nano Lett.*, 2015, **15**, 6490–6493.

43 B. Ding, H. Chen, J. Tan, Q. Meng, P. Zheng, P. a. Ma and J. Lin, ZIF-8 Nanoparticles Evoke Pyroptosis for High-Efficiency Cancer Immunotherapy, *Angew. Chem., Int. Ed.*, 2023, **62**, e202215307.

44 W. Zhang, Z. Liu, J. Zhu, Z. Liu, Y. Zhang, G. Qin, J. Ren and X. Qu, Bioorthogonal Disruption of Pyroptosis Checkpoint for High-Efficiency Pyroptosis Cancer Therapy, *J. Am. Chem. Soc.*, 2023, **145**, 16658–16668.